

---

Article

# Overcoming the pH Dependence of Iron-Based Catalysts and Efficient Generation of High-Valent Ferrite by Constructing a Neutral Microenvironment

Jingwei Chen and Kangping Cui \*

School of Resource and Environmental Engineering, Hefei University of Technology, Hefei 230009, China;  
2022110726@mail.hfut.edu.cn

\* Correspondence: cuikangping@hfut.edu.cn

**Abstract:** The reliance on acidic working environments presents a significant bottleneck in the development and widespread application of peroxyomonosulfate (PMS)-activated high-valent iron-oxo systems and iron-based catalysts. In this study, we present a system of non-homogeneous activation of peroxyomonosulfate that is capable of overcoming the acidic environment in heterogeneous to generate continuous non-radicals for the selective degradation of organic pollutants such as sulfamethoxazole. The system takes advantage of amphiprotic hydroxides to create a homogeneous neutral pH microenvironment at the heterogeneous interface of the catalyst. The generation of the neutral pH microenvironment is capable of inducing the formation of high-valent iron-oxo species and a more stable cycling of iron ions in the iron-based material, promoting sustained catalytic activity. A series of design quenching experiments, electron paramagnetic resonance (EPR) experiments, and three-dimensional excitation-emission matrix fluorescence spectroscopy (3D-EEM) which were conducted to assess the selectivity of FeCo-LDH/PMS under high salt or natural organic conditions, as well as its effectiveness in treating real wastewater. These findings offer a novel approach to overcoming pH limitations and enhancing the selectivity of target pollutants in advanced oxidation processes (AOPs).

Academic Editor: Juan García Rodríguez

Received: 12 March 2025

Revised: 14 April 2025

Accepted: 29 April 2025

Published: 3 May 2025

**Citation:** Chen, J.; Cui, K. Activation of PMS for SMX Degradation by Constructing a Neutral pH Microenvironment Through the Amphiprotic Characterization of FeCoLDH. *Appl. Sci.* **2025**, *15*, 5100. <https://doi.org/10.3390/app15095100>

**Copyright:** © 2025 by the author. Licensee MDPI, Basel, Switzerland. This article is an open access article distributed under the terms and conditions of the Creative Commons Attribution (CC BY) license (<https://creativecommons.org/licenses/by/4.0/>).

## 1. Introduction

Peroxyomonosulfate (PMS) is a representative sulfate-based oxidizing agent, characterized by its distinctive asymmetric structure ( $\text{HO-SO}_4^-$ ). In recent years, peroxyomonosulfate-driven advanced oxidation processes (AOPs) have attracted significant attention due to their effectiveness in pollutant degradation and operational versatility [1–4]. According to previous studies [5], PMS can be activated by ultraviolet (UV) [6], light [7], heat [8], ultrasound [9], basic particulate activated carbon [10], or transition metals (e.g., Fe, Co) [11,12] to produce reactive sulfate radicals ( $\text{SO}_4^{\cdot-}$ ). Among these activation methods, transition metal activation is the most common and efficient [13]. Among transition metals, iron-based catalysts have gained particular prominence due to their abundance, environmental compatibility, and cost-effectiveness. However, many iron-based catalysts face inherent challenges, such as a slow catalytic conversion rate from Fe(III) to Fe(II) and a sig-

nificant pH dependency, which limits their effectiveness to acidic conditions [14]. In practical applications, PMS activation using iron-based catalysts under acidic conditions generates a radical reaction system based on the Fe(II)/Fe(III) cycle, which sequentially produces  $\text{SO}_4^{\cdot-}$  and hydroxyl radicals ( $\cdot\text{OH}$ ) [15]. While these radicals possess strong oxidative capabilities, their high reactivity also makes the system highly susceptible to interference from coexisting anions in wastewater [16]. This susceptibility leads to poor selectivity toward target pollutants, as the radicals readily react with inorganic salts, humic acid (HA), and other matrix components, resulting in reduced oxidant utilization efficiency and increased treatment costs in real-world wastewater applications [17].

To address these limitations, non-radical pathways have emerged as a promising alternative research focus. Among non-radical species in iron-based systems, high-valent iron-oxo species ( $\equiv\text{Fe(IV)}=\text{O}$  and  $\equiv\text{Fe(V)}=\text{O}$ ) have been extensively studied [18]. Although the formation of high-valent iron-oxo species in iron-catalyzed systems was first reported decades ago, their application in PMS-based advanced oxidation processes (AOPs) has only recently gained momentum [19]. For instance, Wang [20] synthesized Fe(II)-hexadecylchlorophthalate ( $\text{FePcCl}_{16}$ ) and demonstrated its ability to activate PMS under sunlight irradiation. This system effectively degraded carbamazepine, with minimal inhibition observed in the presence of common coexisting ions such as  $\text{NaH}_2\text{PO}_4$ ,  $\text{NaHCO}_3$ ,  $\text{MgSO}_4$ ,  $\text{CaSO}_4$ , and  $\text{NaCl}$ , which was attributed to the involvement of  $\equiv\text{Fe}^{4+}=\text{O}$ . While iron-based catalysts capable of generating  $\equiv\text{Fe(IV)}=\text{O}$  have shown high catalytic efficiency across a broad pH range, most studies have predominantly focused on the initial pH of heterogeneous Fenton-like systems, often overlooking the influence of oxidants and reaction dynamics on system pH. This oversight has led to potentially misleading conclusions regarding pH independence [21]. In reality, PMS-induced formation of high-valent iron-oxo species remains constrained by pH conditions [22]. Consequently, the development of iron-based catalysts capable of truly overcoming pH limitations is critical for advancing AOP adoption in pollution control and for deepening our understanding of the underlying reaction mechanisms [23].

In this study, we synthesized Fe-Co-layered double hydroxides (FeCo-LDH) through a simple co-precipitation method by incorporating  $\text{Co(OH)}_2$  into Fe(III)-based catalysts, facilitating the sequential production of high-valent iron-oxo species. By creating a neutral pH microenvironment, the amphiprotic  $\text{Co(OH)}_2$  effectively extended the applicable pH range and mitigated the proton-assisted self-decomposition of  $\equiv\text{Fe(IV)}=\text{O}$ . The catalytic performance of FeCo-LDH was evaluated through the degradation of sulfamethoxazole (SMX), a representative refractory organic pollutant. The results indicated that FeCo-LDH efficiently activated PMS across a wide pH range. Quenching experiments, electron paramagnetic resonance (EPR) spectroscopy, and oxidation reactions of PMSO identified  $\equiv\text{Fe(IV)}=\text{O}$  as the primary active intermediate. Furthermore, the degradation mechanism of SMX was investigated, and potential degradation pathways within this system were proposed. This study provides a novel strategy to overcome pH limitations in PMS-based AOP systems and offers insights into the catalytic oxidation mechanisms for pollutant degradation, thus broadening the scope of AOP applications in environmental remediation.

## 2. Material and Methods

### 2.1. Chemicals and Reagents

Ferric nitrate hydrate ( $\text{Fe}(\text{NO}_3)_3 \cdot 9\text{H}_2\text{O}$ ), Cobalt nitrate hexahydrate ( $\text{Co}(\text{NO}_3)_2 \cdot 6\text{H}_2\text{O}$ ), Peroxymonosulfate (PMS), Sodium sulfate ( $\text{Na}_2\text{SO}_4$ ), Sodium carbonate ( $\text{Na}_2\text{CO}_3$ ), Sodium chloride ( $\text{NaCl}$ ), Sodium nitrate( $\text{NaNO}_3$ ), Potassium thiocyanate (KSCN), Potassium dichromate ( $\text{K}_2\text{Cr}_2\text{O}_7$ ), Sulfamethoxazole(SMX), 4-chlorophenol (4-CP), Bisphenol A (BPA), Phenol, Oxytetracycline (OTC), Norfloxacin (NOR), Rhodamine B (RhB), Atenolol (ATL),

Blue dimethyl sulfoxide (DMSO), Methyl phenyl sulfoxide (PMSO), 5,5-dimethyl pyrrolidine N-oxide (DMPO), 2,2,6,6-tetramethyl-4-piperidino (TEMP), ethanol (EtOH), Tert-butyl alcohol (TBA), Furfuryl alcohol (FFA), Sodium hydroxide (NaOH), and Sulfuric acid ( $H_2SO_4$ ) were purchased from China Chemical Reagent Co, Ltd., Shanghai Macklin Chemical Reagent Co, or Shanghai Aladdin Biochemical Technology Co. All solutions were prepared with distilled water. The pH of the solutions was adjusted using dilute solutions of NaOH or  $H_2SO_4$ . Buffer preparation: HCOOH-NaOH buffer solution (pH = 4.0):  $[HCOOH] = 0.016\text{ mol/L}$ ,  $[NaOH] = 0.005\text{ mol/L}$ . Phosphate buffer (pH 6.96): composed of 0.1 M NaHPO<sub>4</sub> and Na<sub>2</sub>HPO<sub>4</sub>, adjusted to the target pH using NaOH or HCl. Borax buffer (pH = 9.18): [borax] = 0.01 mol/L. All reagents are of analytical grade unless otherwise stated.

## 2.2. Preparation of Catalysts

$Fe(NO_3)_3 \cdot 9H_2O$  and  $Co(NO_3)_2 \cdot 6H_2O$  with different gradient ratios (molar ratios of Fe:Co=1:1, 1:2 and 1:3, respectively) were dissolved together in 100 mL of distilled water, and then homogenized for 20 min using a mechanical stirrer, which was recorded as solution A. Then, alkaline solution B was prepared (containing NaOH (0.35 mol/L) and  $Na(CO_3)_2$  (0.15 mol/L). The pH of solution A was strictly adjusted to 10 using solution B. The resulting precipitate was poured into a hydrothermal vessel at 80 °C and heated for 24 h. Afterwards, the sample was washed several times on a filter using distilled water and ethanol to achieve a neutral pH of 7.0. Finally, the obtained material was dried in an oven at 40 °C until it reached a constant weight, and stored in a desiccator prior to use, to obtain final ratios of Fe:Co of 1:1, 1:2, and 1:3 for FeCo-LDH.

## 2.3. Degradation Experiments

Typical adsorption and degradation experiments were carried out in 250 mL conical flasks. A certain amount of catalyst was added to a pH-adjusted 100 mL OTC solution and mixed thoroughly for 60 min in a constant temperature shaker to determine the adsorption capacity of the material. Subsequently, the peroxyomonosulfate solution was introduced into the reactor. At reaction times of 0, 2, 5, 10, 20, and 40 min, 1 mL of liquid sample was extracted and filtered through a 0.22 µm polyether sulfone membrane filter, followed by the addition of 0.5 mL of methanol to quench the reaction. The samples were then analyzed immediately using high-performance liquid chromatography (HPLC). Three parallel samples were prepared for each experimental condition, and the results were averaged. In this study we selected catalyst type, pollutant concentration, oxidizer dose, and catalyst dose to perform one-way reaction experiments, respectively. And this is used to judge the catalyst's performance. Detailed experimental conditions can be found in Table 1.

**Table 1.** Specific experimental conditions for four different reaction systems (different catalysts, different target pollutant concentrations, different PMS dosages, different catalyst dosages).

Experimental Conditions	Catalyst Type	Initial pH	SMX Concentration (mg/L)	PMS Dosing Amount (mmol/L)	Catalyst Dosage (g/L)
Catalyst type	3 types of catalysts	7	10	0.3	0.1
SMX concentration	FeCo-LDH	7	10, 20, 25, 50	0.3	0.1
PMS dosing amount	FeCo-LDH	7	10	0.1, 0.3, 0.5, 1	0.1
Catalyst dosage	FeCo-LDH	7	10	0.3	0.05, 0.1, 0.2, 0.5

#### 2.4. Characterization

X-ray diffraction (XRD) patterns were measured with a PANalytical X'Pert PRO MPD (Malvern Panalytical, Rotterdam, The Netherlands) using Cu K $\alpha$  radiation in the 2 $\theta$  range of 5–80°, with the operation parameters of 40 kV and 100 mA and Cu K $\alpha$  radiation ( $\lambda = 1.5406 \text{ \AA}$ ). The crystallographic properties of the samples were investigated at a scanning rate of 0.1° 2 $\theta$  s $^{-1}$ . Fourier transform infrared spectroscopy (FT-IR, Thermo Fisher is50, Thermo Fisher, CA, USA) was used to qualitatively analyze the surface functional groups of the catalysts. FTIR spectra were recorded in the range of 400–4000 cm $^{-1}$  using an ATR accessory, with a resolution of 4 cm $^{-1}$  and 32 scans per sample. A nitrogen gas source was connected at 0.2 MPa for 30 min at a flow rate of 10 L/min before and continuously during the test at a flow rate of 2 L/min. X-ray photoelectron spectroscopy (XPS) analysis for elemental composition (Fe, C, Co, N) was performed using an ESCALAB 250Xi spectrometer (Thermo Fisher, Lenexa, KS, USA), and all spectra were calibrated to the C 1s peak at 284.8 eV. The X-ray photoelectron spectroscopy (XPS) studies were performed on a Thermo Scientific K-Alpha+ system with Al K $\alpha$  radiation operated at 15 KV. The morphological structure of the material was analyzed using field emission transmission electron microscopy. Field emission transmission electron microscopy (TEM, JEM-2100F, JEM, Osaka, Japan) was performed with a ZrO/W(100) Schottky thermal field emission electron gun at an accelerating voltage of 200 kV. All electrochemical characterizations were performed using a typical three-electrode cell in an Autolab PGSTAT302N(Metrohm Autolab, Zürich, Swiss). A platinum wire was used as the counter electrode and Ag/AgCl was used as the reference electrode. The working electrode was prepared by dropping 7  $\mu\text{L}$  of ink catalysts, previously prepared by thoroughly mixing 10 mg of catalysts with 10 mg of conductive carbon (Vulcan) and 1 mL absolute ethanol and 0.1 mL Nafion solution (5 wt%), on a glassy carbon rod 4 mm in diameter. Chronoamperometry was conducted in 100 mL Na<sub>2</sub>SO<sub>4</sub>(0.1M) as an electrolyte solution with 0.0 V bias potential vs. Ag/AgCl reference electrode for a total time of 1200 s. Electrochemical impedance spectroscopy (EIS) was performed with a 10 mV amplitude perturbation and a frequency range of 0.01–100 kHz. Cyclic voltammetry (CV) was performed in a potential range from −0.6 V (vs. Ag/AgCl) to 1.0 V (vs. Ag/AgCl) at a scan rate of 50 mV/s. Cyclic voltammetry (CV) and electrochemical impedance spectroscopy (EIS) measurements were carried out on an electrochemical workstation (CHI7602, Chenhua, Shanghai, China).

#### 2.5. Analysis Method

Determination of SMX and methyl phenyl sulfone (PMSO) was performed using HPLC (LC-20A, Shimadzu Corporation, Fukuoka, Japan). The iron and cobalt content was determined using an atomic absorption spectrophotometer (AA-800, Perkin Elmer, CA, USA). Free radical detection was conducted using electron spin resonance (ESR, JEOL JES-FA200, JEOL Ltd., Osaka, Japan). The degradation products of pollutants were analyzed using an orbitrap-based high-resolution liquid chromatography-mass spectrometer (UHPLC-Q Exactive Plus, Thermo Fisher Scientific Co, USA). Three-dimensional fluorescence spectroscopy (3D-EEM) was employed to detect the degradation of non-radical species in real water bodies ((LS-55, Perkin-Elmer Co., USA). All the details of the analytical methodology can be found in Text S1.

### 3. Results and Discussion

#### 3.1. Characterization of Catalysts

The co-precipitation method involves mixing solutions of metal salts at specific concentrations in predetermined proportions. A base solution, typically sodium hydroxide (NaOH), is gradually added dropwise to the combined salt solution to adjust its pH. After

an aging process with continuous stirring, the resulting product is filtered, cleaned, and dried. During aging,  $\text{Fe(OH)}_3$  and  $\text{Co(OH)}_2$  formed in the solution are incorporated into the layered double hydroxide (LDH) structure, which can be chemically expressed as  $[\text{M}_1^{2+}\text{M}_2^{\oplus}(\text{OH})_2(\text{A}_n^-)_x]^{x+}\text{mH}_2\text{O}$  [24]. In this expression,  $\text{M}^{2+}$  and  $\text{M}^{\oplus}$  represent  $\text{Co}^{2+}$  and  $\text{Fe}^{\oplus}$ , respectively, while the interlayer anion  $\text{A}_n^-$  is  $\text{CO}_3^{2-}$  in this work. Figure 1a presents the X-ray diffraction (XRD) patterns of FeCo-LDHs with  $\text{Fe}^{\oplus}/\text{Co}^{2+}$  molar ratios of 1:1, 1:2, and 1:3. According to previous reports [25], typical LDHs exhibit a strong absorption peak at low angles and two weaker, equally spaced peaks at intermediate angles, along with two relatively weak peaks near  $60^\circ$ . The characteristic peaks of LDH (JCPDS 50-0235) are observed at  $11.75^\circ$ ,  $23.57^\circ$ ,  $34.11^\circ$ ,  $38.76^\circ$ ,  $46.28^\circ$ , and  $60.70^\circ$ , indicating that LDHs with a high  $\text{Fe}/\text{Co}$  ratio exhibit better crystalline structures. However, for a  $\text{Fe}^{\oplus}/\text{Co}^{2+}$  ratio of 1:1, the characteristic peaks were significantly weakened or absent, suggesting that excessively higher  $\text{Fe}^{\oplus}/\text{Co}^{2+}$  ratios are unfavorable for forming well-defined LDH structures.

Fourier-transform infrared (FTIR) spectroscopy was conducted to identify the functional groups, chemical bonding states, and interlayer anions present in the LDHs. Samples were dried and measured in powder form. Figure 1b shows the FTIR spectra of Fe-Co (1:1), Fe-Co (1:2), and Fe-Co (1:3) samples, which exhibit similar curves. An intensive band between  $3427$  and  $3503 \text{ cm}^{-1}$  corresponds to the stretching vibrations of hydroxyl groups within hydroxymagnesite-like layers [26]. The strong peak at  $1634 \text{ cm}^{-1}$  is attributed to the deformation mode of interlayer water molecules, confirming the presence of hydroxyl groups and water in the samples [27,28]. Various interlayer anions are characteristic of LDHs, and their host-guest affinities follow the order:  $\text{CO}_3^{2-} > \text{SO}_4^{2-} > \text{OH}^- > \text{F}^- > \text{Cl}^- > \text{Br}^- > \text{NO}_3^- > \text{I}^-$  [29]. The absorption peak at  $1356 \text{ cm}^{-1}$  corresponds to the vibrational absorption of interlayer  $\text{CO}_3^{2-}$  [30], suggests that  $\text{CO}_3^{2-}$  is one of the LDH interlayer anions. Additionally, spectral bands in the range of  $1000$ – $400 \text{ cm}^{-1}$  are associated with metal-oxygen (M–O) or metal-hydroxyl (M–OH) vibrations [31]. Peaks at  $732 \text{ cm}^{-1}$  correspond to Co–OH mode [32].

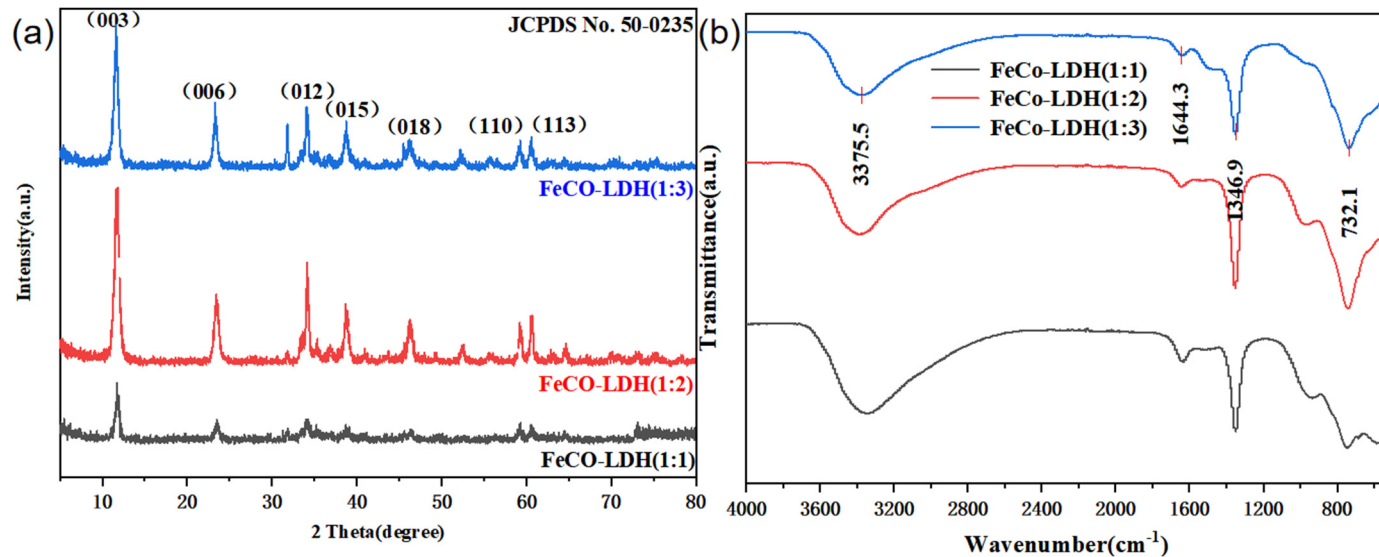


**Figure 1.** (a) XRD patterns of different catalysts; (b) FTIR spectra of different materials (different ratios of iron to cobalt).

As shown in Figure 2, the morphological characteristics of Fe-Co (1:3) samples were systematically investigated by transmission electron microscopy (TEM). Layered double hydroxides (LDHs) typically exhibit octahedral symmetry, where the metal cations are located at the centers of the octahedral units and the hydroxide anions occupy the vertices.

These structural units are interconnected by edge sharing to form extended two-dimensional coordination layers, resulting in the characteristic lamellar structure of LDHs [33,34]. TEM images (Figure 2a,b) clearly show the presence of lamellar, layered morphology [34]. In addition to this, a less organized structure is shown, with the lamellae being partially fragmented and irregular. This deviation from the ideal crystalline morphology may be due to the inhomogeneity of the local alkali concentration during the synthesis process, possibly due to insufficient reaction time or unsatisfactory stirring, resulting in localized corrosion of the otherwise well-dispersed hexagonal nanosheets. Combined with XRD and FT-IR analyses, these observations confirm the successful synthesis of the LDH structures, thus validating their applicability for subsequent catalytic or physico-chemical applications.

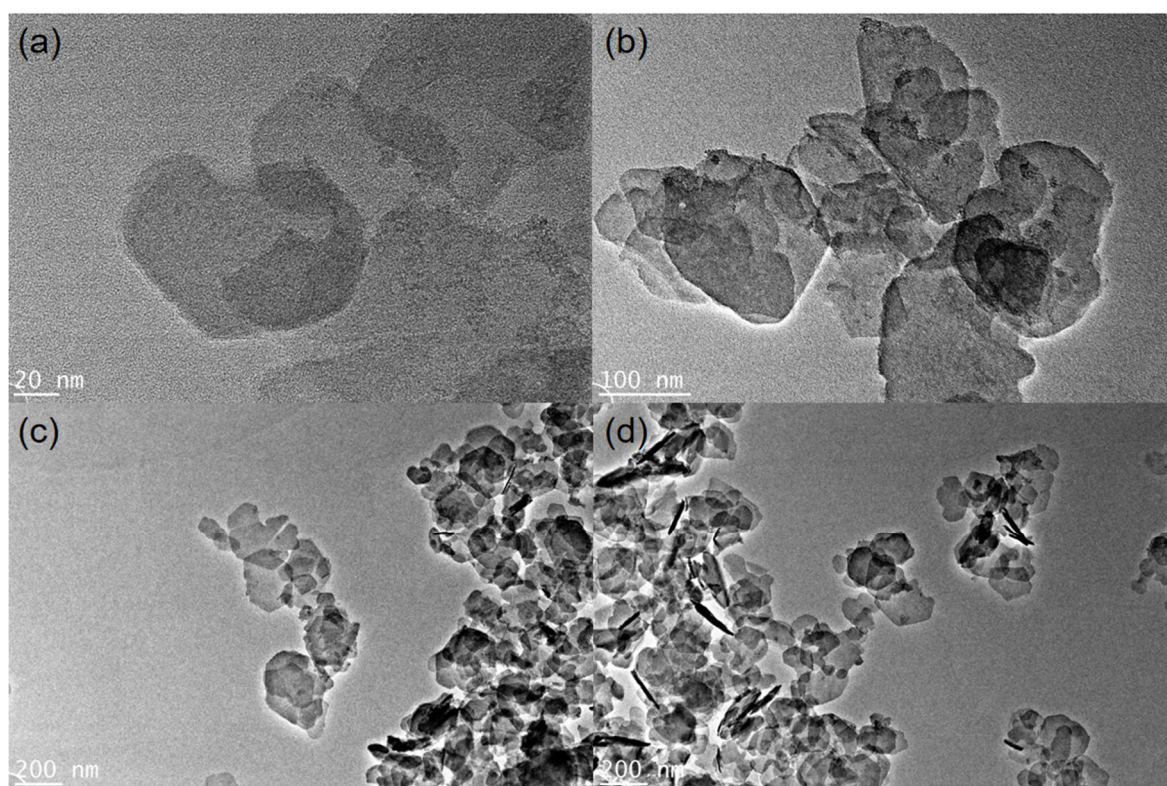


**Figure 2.** (a–d) TEM image of the material at different magnifications.

X-ray photoelectron spectroscopy (XPS) analysis was used to determine the elemental composition and chemical state of the catalyst surface. As shown in Figure 3a, FeCo-LDH (1:3) samples were successfully incorporated with iron and cobalt elements. In the Fe 2p spectra (Figure 3b), the peaks at 711.0 eV and 722.7 eV demonstrate the presence of  $\text{Fe}^{2+}$ , while the peaks at 712.9 eV and 726.2 eV indicate the presence of  $\text{Fe}^{3+}$  [35,36]. In the Co 2p spectra (Figure 3c), the main peaks at 781.8 eV corresponding to Co 2p<sub>3/2</sub> and at 798.4 eV for Co 2p<sub>1/2</sub>, as well as the satellite bands at 787.4 eV and 803.7 eV, are in accordance with the reported values of  $\text{Co(OH)}_2$ . The peaks at 799.8 and 784.0 eV correspond to Co(II), while the peaks at 797.8 and 803.7 eV correspond to Co(III), which confirms the coexistence of  $\text{Co}^{2+}$  and  $\text{Co}^{3+}$  states [37]. The C1s spectrum (Figure 3d) shows peaks at 284.7, 286.7, and 289.4 eV corresponding to C-C, C-O, and C=O bonds. It was shown in [38] that the C=O group contributes to the decomposition of PMS to generate single linear oxygen, which was further confirmed in subsequent experiments. These results indicate that the metallic elements Fe and Co are already present in the obtained material.

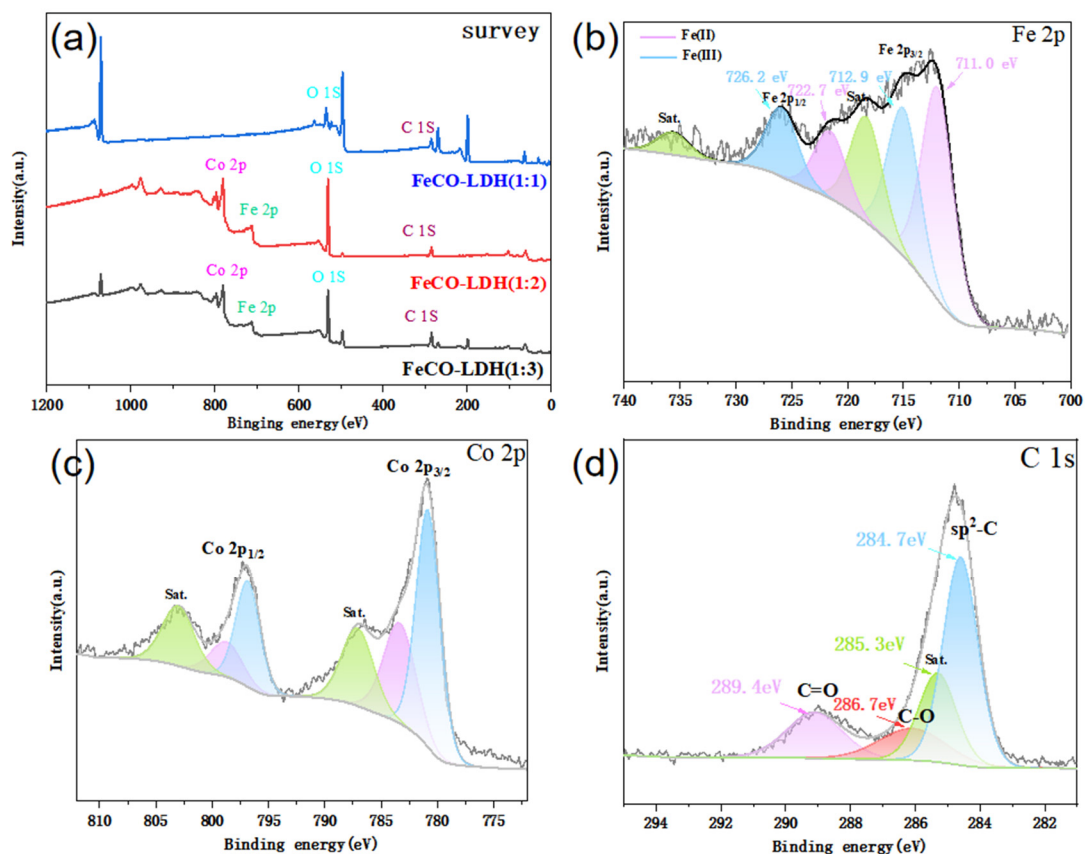


**Figure 3.** (a) XPS patterns of different catalysts; (b) High-resolution Fe 2p spectra of catalyst; (c) High-resolution Co 2p spectra of catalyst; (d) High-resolution C 1s spectra of catalyst.

Electrochemical tests were conducted to evaluate electron transfer efficiency. Cyclic voltammetry (CV) curves (Figure 4a) show that FeCo-LDH (1:3) exhibited the highest peak current density, indicating superior reversibility and ionization potential compared to other samples. The charge transfer resistance is obtained from the Nyquist plot (real part ‘Z’ vs. imaginary part “Z”) in electrochemical impedance spectroscopy (EIS), which is characterized as a semicircle in the plot. Usually, the diameter of the semicircle corresponds to the charge transfer resistance. The real part of the impedance in the high frequency region, Z2’, is usually the first data point or the region that is initially close to horizontal. The impedance real part Z1’ in the low frequency region is the horizontal inflection value at the end of the semicircle. The charge transfer resistance is calculated as  $R_{ct} = Z2' - Z1'$  [39,40]. The electrochemical impedance spectroscopy (EIS) results further support the CV analysis by providing insight into the interfacial charge transfer kinetics. As shown in Figure 4b, the charge transfer resistance ( $R_{ct}$ ), approximated from the diameter of the Nyquist semicircles, decreased significantly with increasing Co content. The  $R_{ct}$  values for FeCo-LDH (1:1), (1:2), and (1:3) were estimated to be ~3950, ~1860, and ~870  $\Omega$ , respectively, indicating that FeCo-LDH (1:3) facilitates the most efficient electron transport among the three compositions. These findings suggest that an optimized Fe/Co ratio enhances the catalytic activity by improving electron mobility and reducing interfacial resistance [41,42].

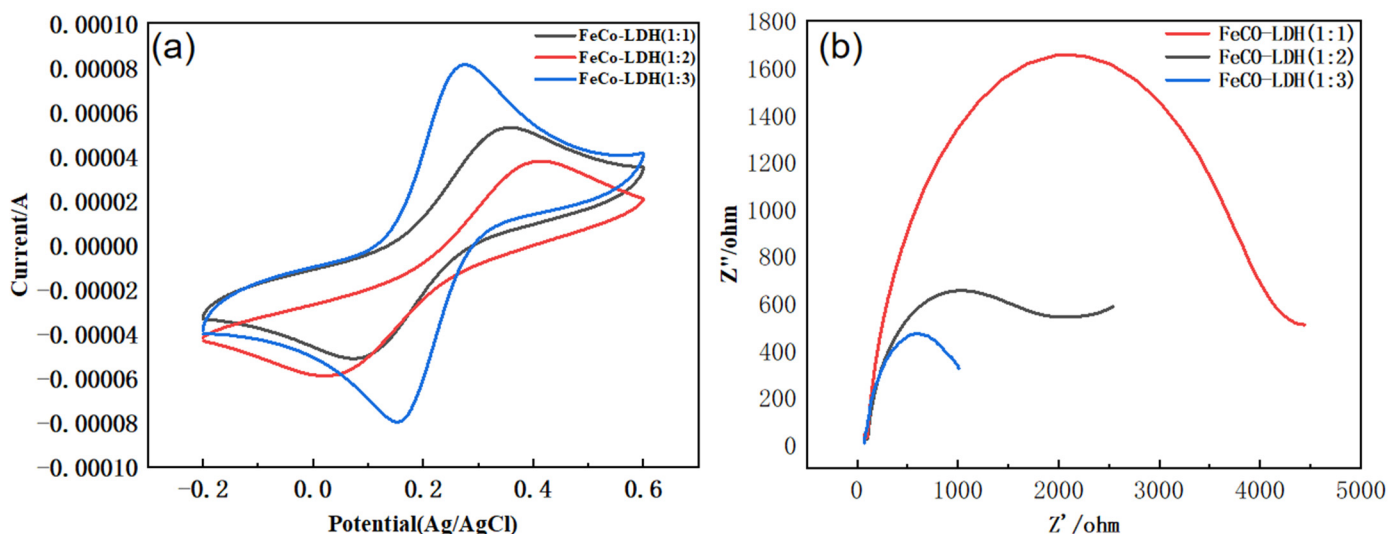


**Figure 4.** CV (a) and EIS (b) patterns of different catalysts.

### 3.2. Effective Activation of PMS with Catalysts for Contaminant Removal

To thoroughly evaluate the catalytic performance of the prepared FeCo-LDH catalysts for degrading organic pollutants via PMS activation, their efficiency in degrading sulfamethoxazole (SMX) was examined under controlled conditions (catalyst dosage: 0.1 g/L; PMS: 0.3 mmol/L; pH: 6.96; SMX concentration: 10 mg/L). As depicted in Figure 3a, PMS alone exhibited a minimal SMX degradation rate of only 6.99%, with an apparent reaction rate constant of  $0.0443 \text{ min}^{-1}$ . However, the catalytic activity improved significantly with an increase in the  $\text{Co}^{2+}/\text{Fe}^{3+}$  ratio. The basic structure of LDHs is represented as  $[\text{M}_{1-x}^{2+}\text{M}_x^{3+}(\text{OH})_2(\text{A}_n^-)_x/n]\text{x}^+\cdot\text{mH}_2\text{O}$ . The observed variation in catalytic performance suggests that the optimal  $\text{M}^{2+}/\text{M}^{3+}$  ratio for LDHs lies between 1 and 3, aligning with previous findings that the synthesis of LDH compounds is most effective when  $0.2 \leq x \leq 0.33$  [43,44]. The XPS images of LDH with different iron to cobalt ratios illustrate the conclusion just made very well (Figures S1–S4), as the peaks represented by iron are completely absent from the Fe2p spectra of the material at the 1:1 ratio, while the elemental peaks of the material at the other two ratios are well presented. Additional experiments investigated the influence of catalyst dosage and SMX concentration on degradation efficiency, with detailed results provided in the Supplementary Information (Figures S5–S7).

As shown in Figure 5b, the degradation rate of the system for SMX was 79.2% at an initial pH of 3, and reached nearly 100% at an initial pH of 11, with the degradation rate showing a decreasing trend with increasing pH. Notably, the degradation efficiency remained high regardless of the initial pH. During the reaction, the system's pH quickly stabilized between 4.0 and 6.96 within 10 min after the catalyst addition, regardless of initial pH levels. This behavior contrasts with PMS alone, which cannot neutralize the solution pH due to its intrinsic acidity [45]. The observed pH stabilization is likely attributed to the presence of  $\text{Co}(\text{OH})_2$  in the catalyst. When the  $\text{M}^{2+}/\text{M}^{3+}$  ratio in LDHs falls within the range of 0.5–2, the proximity of  $\text{M}^{3+}(\text{OH})_3$  octahedra facilitates the formation of  $\text{M}(\text{OH})_3$ . Conversely, when  $x < 0.33$ , hydrotalcite-like layers predominantly generate  $\text{M}(\text{OH})_2$  instead [46]. The sequential reactions between  $\text{Co}(\text{OH})_2$  on the catalyst surface and  $\text{H}^+$  or  $\text{OH}^-$  ions in the solution drive the system's pH toward neutrality. To further confirm the broad pH adaptability of FeCo-LDH, different buffer systems were employed to maintain stable pH conditions during the reaction. Specifically,  $\text{HCOOH}-\text{NaOH}$  ( $\text{pH} = 4.0$ ), phosphate ( $\text{pH} = 6.96$ ), and borax ( $\text{pH} = 9.18$ ) buffer solutions were used. Detailed buffer compositions are provided in the methods section. Figure 5d illustrates the degra-

dation trends and pH changes of SMX under various buffered conditions. The results reveal differences in SMX degradation efficiency depending on the pH environment. While acidic conditions initially exhibit faster degradation rates, neutral pH conditions achieve superior overall efficiency. Conversely, alkaline conditions provide more sustained degradation, albeit at a slower initial rate. These findings underscore the robust performance of Fe-Co LDHs across diverse pH environments, with neutral conditions being particularly effective for pollutant degradation.

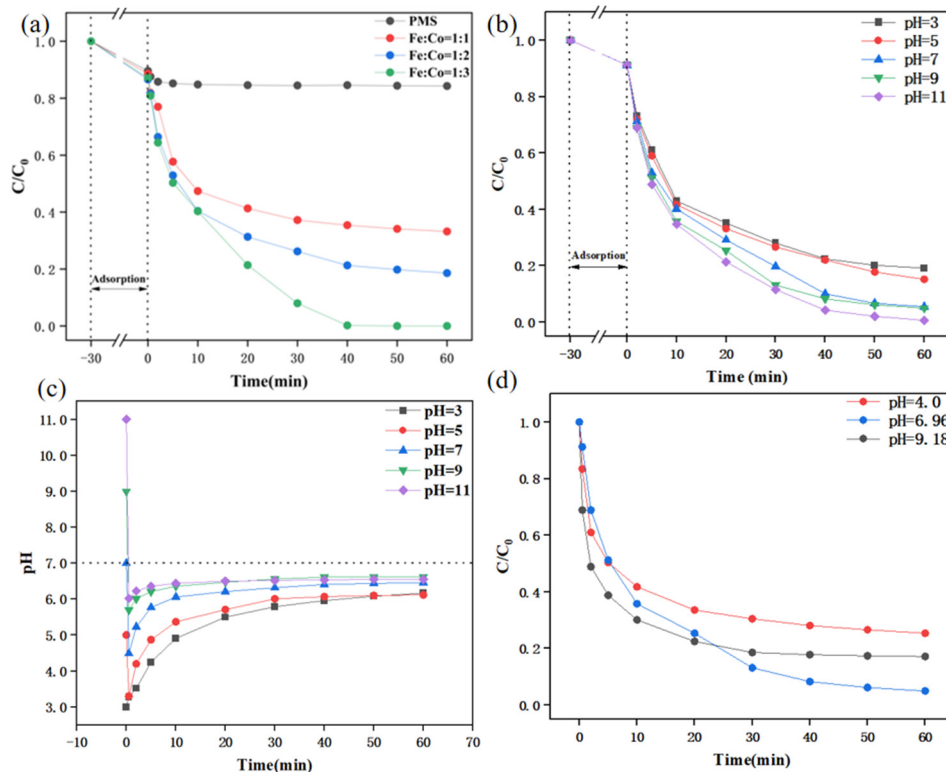


**Figure 5.** (a) Degradation of SMX under various systems (Catalyst concentration: 0.1 g/L, SMX concentration: 10 mg/L, PMS concentration: 0.3 mmol/L, pH ≈ 5.6, Temperature = 25 °C); (b) Effect of different initial pH values on SMX degradation using the FeCo-LDH + PMS system (Catalyst concentration: 0.1 g/L, SMX concentration: 10 mg/L, PMS concentration: 0.3 mmol/L, pH values: 3.0, 5.0, 7.0, 9.0, and 11.0, Temperature = 25 °C); (c) pH variation trends throughout the process under different initial pH conditions; (d) Buffer solutions and pH changes during the reaction (Catalyst concentration: 0.1 g/L, SMX concentration: 10 mg/L, PMS concentration: 0.3 mmol/L, pH values: 4.0, 6.86, and 9.18, Temperature = 25 °C).

Figure 6 highlights that cobalt leaching peaks during the first 10 min of the reaction, coinciding with the stabilization of the pH. Materials with elemental cobalt as the main catalytic site often show strong leaching in peroxymonosulfate systems due to the self-generated acidic environment of PMS [47], and the excess H<sup>+</sup> under acidic conditions scavenges -OH in the environment to reduce the degradation rate. In contrast, the concentrations of Fe and Co ions in the leachate were lower than 0.2 mg/L in the five cycling experiments. These values were much lower than the permissible threshold (1 mg/L) specified by the Chinese national standard (GB 25467-2010) [48], which further illustrated the adaptability of the material to different environments.

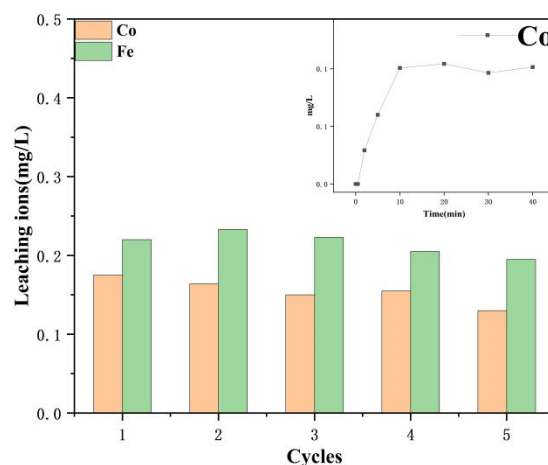


**Figure 6.** Metal ion leaching rates across five reactions.

### 3.3. Reactive Oxygen Species During PMS Activation

To confirm the reactive species in the FeCo-LDH/PMS system, scavenging experiments were conducted to evaluate the roles of both radical and non-radical species (Figure 7a). For conventional radicals such as  $\cdot\text{OH}$ ,  $\text{SO}_4^{\cdot-}$ , and  $\text{O}_2^{\cdot-}$ , quenchers including tert-butanol (TBA), methanol (MeOH), and p-benzoquinone (p-BQ) were used. Additionally, TBA and ethanol (EtOH) helped differentiate the high-valent contributions of  $\cdot\text{OH}$  and  $\text{SO}_4^{\cdot-}$  [49]. For non-radical species, dimethyl sulfoxide (DMSO) and furfuryl alcohol (FFA) were employed as specific quenchers. DMSO selectively quenches iron oxides that degrade SMX [50], while FFA assesses the contribution of singlet oxygen ( $^1\text{O}_2$ ). The quenching effects revealed that free radical inhibitors reduced degradation rates modestly (1.7%, 3.5%, and 18.1% for TBA, MeOH, and p-BQ, respectively), while non-radical inhibitors had a more pronounced impact: FFA reduced the rate by 42.3%, and DMSO nearly halted the reaction. These results indicate that high-valent iron oxides were the primary reactive species, accompanied by smaller contributions from  $^1\text{O}_2$  and  $\text{O}_2^{\cdot-}$ .

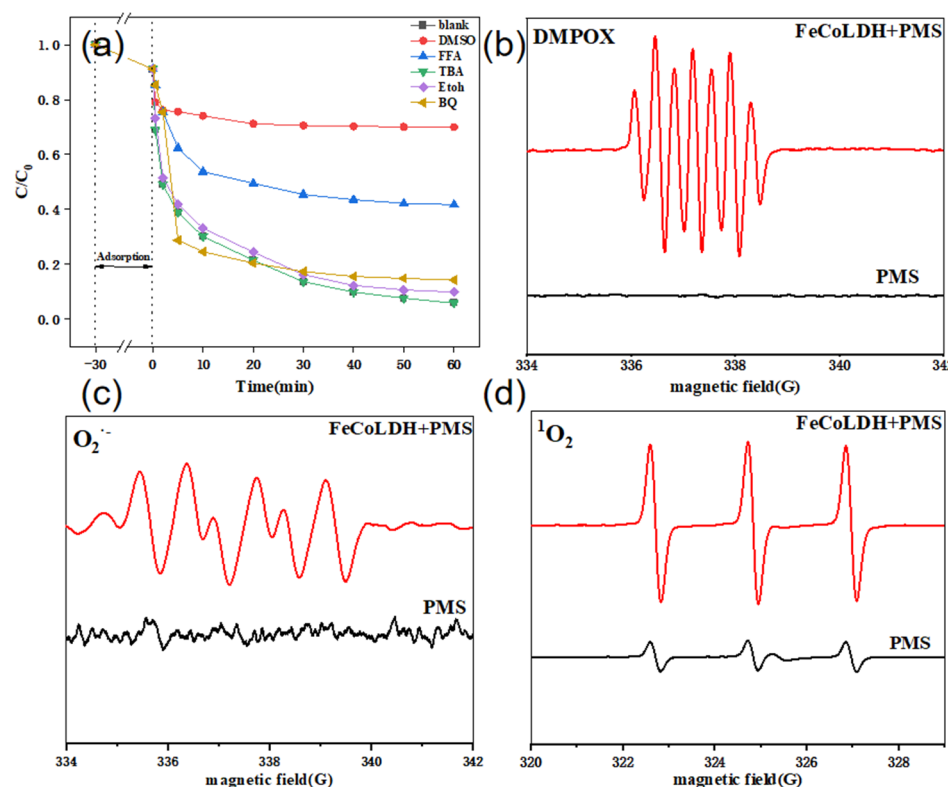


**Figure 7.** (a) Effect of free radical scavengers on SMX degradation in FeCo-LDH/PMS system; (b–d) EPR mapping in different catalytic systems.

Electron spin resonance spectroscopy (ESR) measurements were carried out using 5,5-dimethyl-1-pyrrolidine-N-oxide (DMPO) [51] and 2,2,6,6-tetramethyl-4-piperidone (TEMP) [52] as spin trapping agents to qualitatively and semi-quantitatively assess radical and non-radical species in the FeCo-LDH/PMS reaction system. In aqueous solutions, no DMPO-OH or DMPO-SO<sub>4</sub><sup>·-</sup> signals were observed. In contrast, upon addition of FeCo-LDH and PMS, a seven-line spectrum with an intensity pattern of 1:2:1:2:2:1:2:1 was observed, identified as 5,5-dimethylpyrrolidone-2(oxy)-1 (DMPX). This indicates the presence of strong oxidizing intermediates in the system. These intermediates are most likely high-valent iron species such as Fe(IV) or Fe(V), which are known to play a role in oxidation processes involving iron-based catalysts [53]. In order to further verify the presence of high-valent iron species, we will conduct further quenching experiments on them in the following. Moreover, peaks related to DMPO-O<sub>2</sub><sup>·-</sup> in ethanol confirmed the involvement of free radicals in the reaction [54,55]. TEMP-captured signals of <sup>1</sup>O<sub>2</sub> revealed higher intensities in the FeCo-LDH/PMS system compared to PMS alone, further supporting the presence of <sup>1</sup>O<sub>2</sub> during activation [56]. High-valent iron oxides exist in multiple forms, including Fe(V)=O, Fe(IV)-OH, and Fe(IV)=O [57].

The formation of PMSO<sub>2</sub> from PMSO via oxygen atom transfer by Fe(IV)=O was used to detect its presence [58]. HPLC-MS chromatograms of standard PMSO and oxidized PMSO in the FeCo-LDH/PMS system (Figure 8a,b) showed selective conversion to PMSO<sub>2</sub>, with a prominent peak (*m/z* = 157.03) at 3.13 min. This confirmed Fe(IV)=O as a key intermediate. The molar ratio of PMSO<sub>2</sub> formed to PMSO consumed exceeded 85.3% throughout the reaction (Figure S9), indicating that high-valent iron oxides predominantly drove SMX degradation, while <sup>1</sup>O<sub>2</sub> and O<sub>2</sub><sup>·-</sup> contributed through secondary pathways.

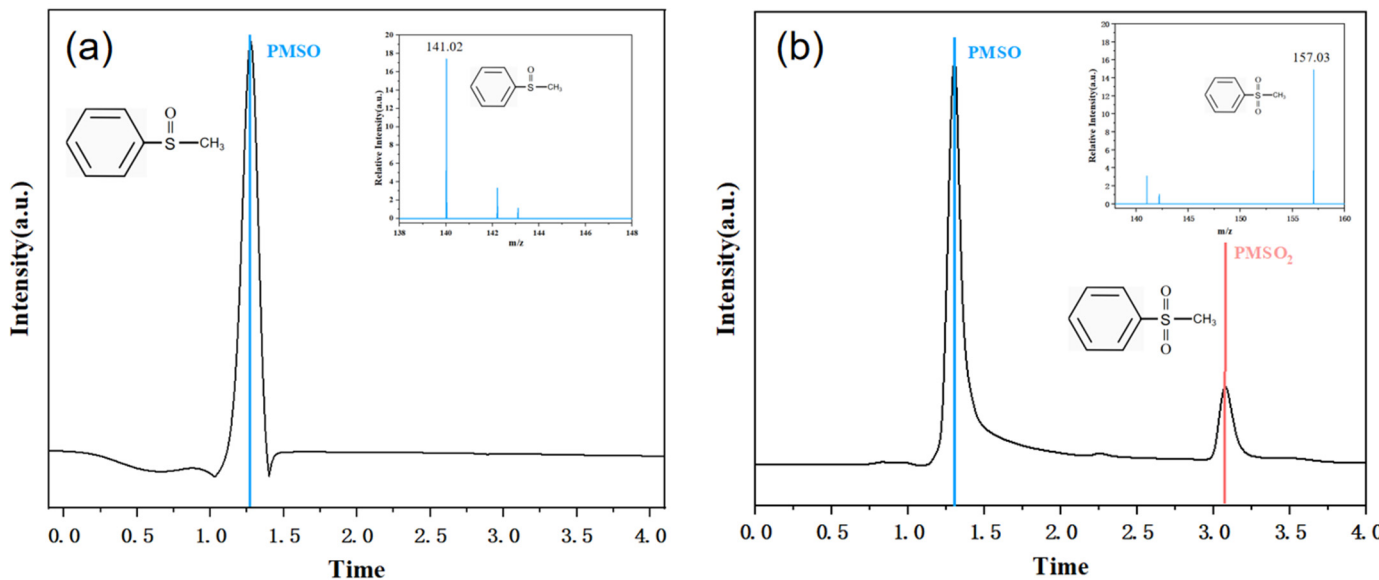


**Figure 8.** (a,b) High-performance liquid chromatography/electrospray ionization tandem mass spectrometry full-scan chromatogram and the molecular ion mass spectra of PMSO and PMSO<sub>2</sub> before and after the catalytic reaction.

Further investigation revealed electron transfer between Fe(III) and Co(II), with ≡Fe(IV)=O derived directly from Fe(III) rather than via Fe(II) [59]. Quenching experiments

using 1,10-phenanthroline and KSCN confirmed this mechanism. While 1,10-phenanthroline had minimal impact on SMX degradation, KSCN significantly inhibited the reaction at higher concentrations, suggesting that SCN<sup>-</sup> strongly coordinates with Fe(III), preventing the formation of Fe(IV)=O. These findings highlight the central role of Fe(III) active sites in FeCo-LDH during the catalytic process. To determine whether high-valent iron oxides were surface-complexed or free in solution, potassium dichromate (K<sub>2</sub>Cr<sub>2</sub>O<sub>7</sub>) was used as an electron scavenger. Minimal inhibition of SMX removal (Figure 9a) indicated that the degradation mechanism likely relied on direct electron transfer from the catalyst surface. The structural formula of LDH, [M<sub>x</sub><sup>2+</sup>M<sub>y</sub><sup>3+</sup>(OH)<sub>2</sub>(A<sub>n</sub><sup>-</sup>)<sub>x</sub>/n]x<sup>+</sup>·mH<sub>2</sub>O, suggests that M(III) sites within the layered structure act as catalytic active centers.

In conclusion, FeCo-LDH activates PMS by forming high-valent iron-oxo species, which are crucial intermediates for SMX degradation. Chronoamperometric studies confirmed this electron transfer mechanism. No current response was observed upon adding SMX alone, but introducing PMS induced a sharp current increase, signifying electron transfer from surface M<sup>3+</sup> sites to PMS. Subsequently, SMX addition reversed the current direction, indicating electron transfer from SMX to the catalyst, thus driving its degradation [60].

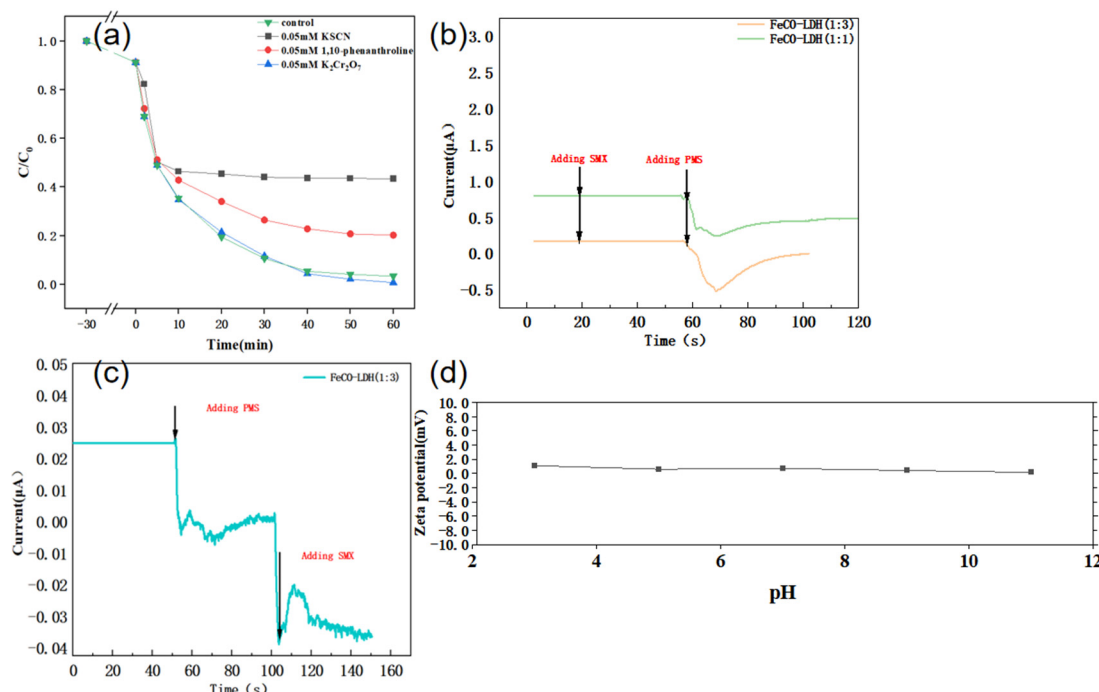


**Figure 9.** (a) Effect of SCN<sup>-</sup>, 1, 10-phenanthroline and K<sub>2</sub>Cr<sub>2</sub>O<sub>7</sub> on the degradation of SMX by FeCo-LDH/PMS system; (b,c) Continuous injection of SMX and PMS current reactions on catalysts' working electrodes; (d) Zeta potential of catalyst at different pH.

The variation of zeta potential in acidic, neutral, and alkaline solutions is influenced by both the pH of the solution and the charge characteristics of the colloidal particle surface. Under acidic conditions, i.e., a low pH environment, there is a higher concentration of H<sup>+</sup> in solution, which promotes protonation of surface groups. For example, metal oxides usually have positively charged surfaces with positive zeta potentials when hydroxyl groups (-OH) are present on the surface [61]. Organic substances such as humic acids and fulvic acids are usually negatively charged under neutral to alkaline conditions. This is because their functional groups such as carboxyl and phenolic hydroxyl groups are deprotonated under neutral or alkaline conditions, resulting in the formation of a negative

charge [62]. In contrast, in neutral solutions, the concentrations of hydrogen and hydroxide ions are relatively balanced, and the particle surface charge is typically more stable at this pH [63]. We measured the  $\zeta$ -potential of the catalyst at different pH values (Figure 9d) and found that the  $\zeta$ -potential remained around 0 mV in the pH range of 3–9, indicating that the charge on the particle surface remains stable over a wide pH range. This phenomenon is likely due to cobalt hydroxide on the surface of the material, which neutralizes a significant number of hydrogen ions in the solution, driving the solution's pH toward neutrality. Furthermore, based on the unique structure of layered double hydroxides (LDHs), the octahedral sites can readily accommodate Co(II), Co(III), Fe(II), and Fe(III). This structure allows Fe and Co species to reversibly undergo redox reactions while maintaining the overall structure, in addition to neutralizing the pH and generating reactive species [64].

The degradation products of sulfamethoxazole (SMX) at different pH values were examined using LC-MS (Figure S10). The main degradation intermediates identified were TP-187, TP-129, TP-99, and TP-158. Among these, TP-99 and TP-158 were formed through the cleavage of sulfonamide (S-N) bonds (Figure 10). Previous studies have shown that the S-N bond in SMX is particularly susceptible to attack by free radical species such as  $\text{SO}_4^{\cdot-}$ ,  $\text{O}_2^{\cdot-}$ , etc. [65,66]. Additionally, TP-187 and TP-129 undergo further oxidation of the  $-\text{NH}_2$  group to form  $-\text{NO}_2$ , while TP-114 is generated by the oxidation of the  $-\text{CH}_3$  group in TP-99 to  $-\text{CHO}$ . The non-radical selectivity of these reactions makes them highly reactive toward electron-rich groups such as sulfonamides. Most of the degradation products are formed by the oxidation of groups on the sulfonamide. Notably, the coupling product TP-503, resulting from the formation of an N=N bond between two SMX molecules, was detected in the system [67]. Figure 10 illustrates several major degradation pathways of SMX, which can be broadly categorized into hydrogen substitution, oxidation, and coupling.

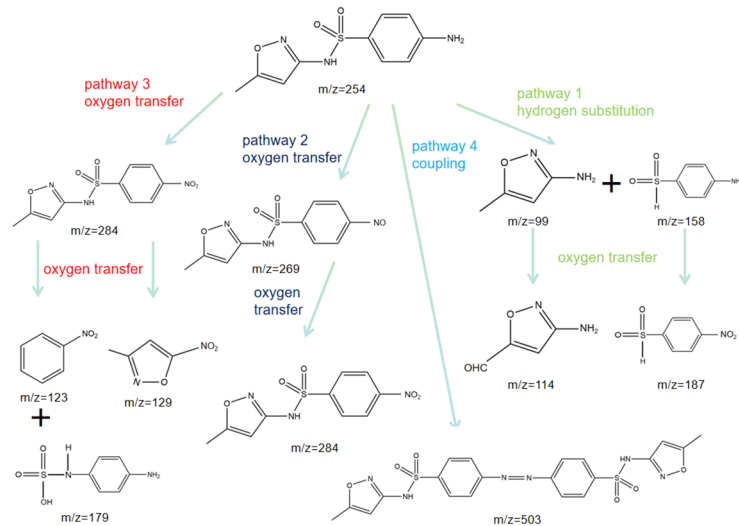
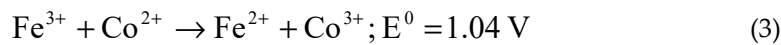
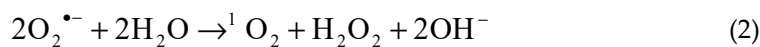


**Figure 10.** Possible degradation pathways of SMX.

In conclusion, the possible mechanism in the FeCo-LDH/PMS system was proposed as follows: In the current study, there are three main pathways for the generation of the non-radical species  ${}^1\text{O}_2$ , which are the autodecomposition of peroxy monosulfate [68], the reaction between  $\text{O}_2^{\cdot-}$  and  $\cdot\text{OH}$  [69], and the disproportionation of  $\text{O}_2^{\cdot-}$  [70]. In the EPR test experiments and quenching experiments in the paper, we confirmed that  $\text{O}_2^{\cdot-}$  is indeed present in the system, but not  $\cdot\text{OH}$ , so the reaction between  $\text{O}_2^{\cdot-}$  and  $\cdot\text{OH}$  is ruled out first. Secondly, in the PMS-only system, we detected the presence of  ${}^1\text{O}_2$  by EPR, so there may be a generation pathway by deprotonated autolysis of peroxymonosulfate [71] (Equation (1)). The presence

of  $\text{O}_2^-$  and the further generation of  ${}^1\text{O}_2$  in the system after addition of the catalyst suggests that there may be the disproportionation of  $\text{O}_2^-$  (Equation (2)). The octahedral coordination geometry in LDHs' layered structure enables facile incorporation of multivalent cobalt ( $\text{Co}^{2+}/\text{Co}^{3+}$ ) and iron ( $\text{Fe}^{2+}/\text{Fe}^{3+}$ ) species, permitting reversible redox cycling without structural degradation. Thermodynamic evaluations through standard reduction potentials (Equation (3)) reveal energetically favorable electron transfer between Co(II) and Fe(III) redox couples [72]. Fe(III) sites in FeCoLDH first coordinated with the O atoms in PMS and formed  $[\text{Fe}(\text{III})\text{OOSO}_3]^+$  complexes (Equation (4)) [60]. The major active  $\equiv\text{FeIV}=\text{O}$  species were formed from the heterolytic cleavage of O-O in  $[\text{Fe}(\text{III})\text{OOSO}_3]^+$  complexes, and since the presence of  $\text{SO}_4$  was not found within the system, the complex cleavage may need to be carried out with a reducing substance, which, based on the properties of the material, is likely to be divalent Fe or Co [73,74].



### 3.4. FeCo-LDH System Application

The cycling performance of catalyst materials is a crucial factor in assessing their potential for practical applications. The results (Figure 11a) demonstrated that the catalytic efficiency of FeCo-LDH remained exceptionally high after five reaction cycles under consistent conditions. Additionally, the presence of inorganic anions ( $\text{Cl}^-$ ,  $\text{SO}_4^{2-}$ , and  $\text{NO}_3^-$ ) had minimal impact on the degradation of SMX in the FeCo-LDH/PMS system (Figure S11), further confirming the catalyst's suitability for real-world water purification. Finally, we selected three phenolic pollutants as well as three antibiotics for degradation to examine the applicability of the materials, and the results, as shown in Figure 11b, achieved more than 85% removal for all six pollutants.

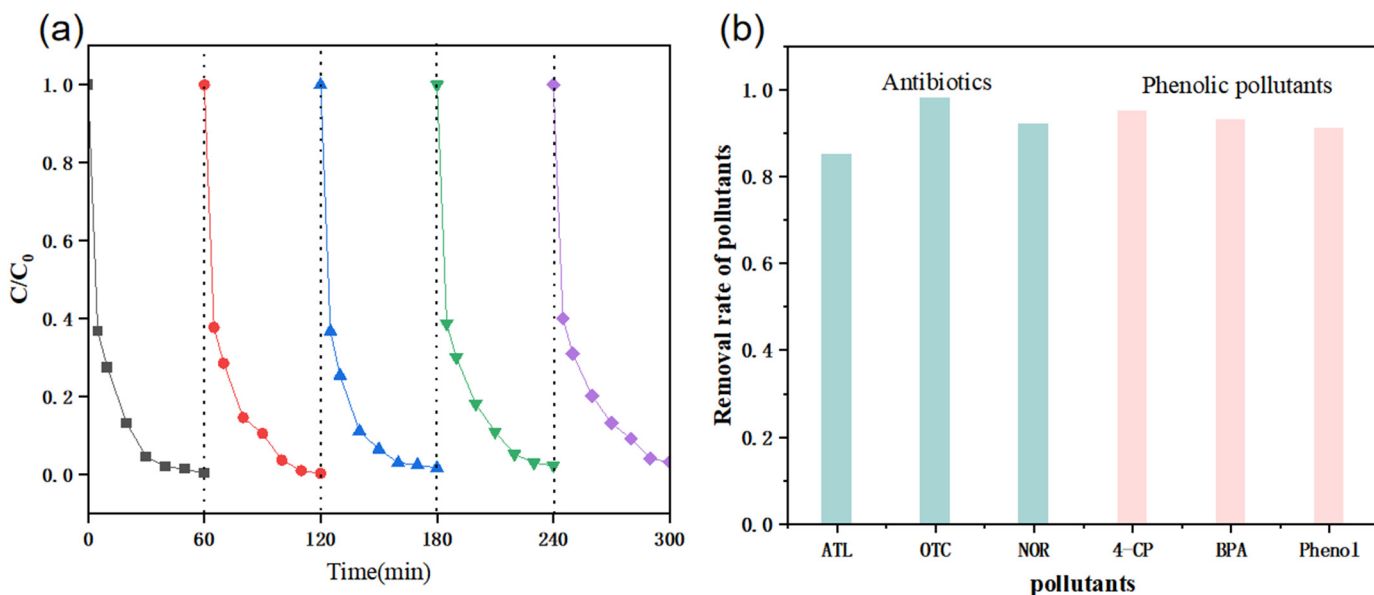


**Figure 11.** (a) Recycling performance of catalyst; (b) Removal of different pollutants by catalyst.

In order to examine the degradation of the target pollutant in a real water body, polluted wastewater from a real sewage plant was selected and the target pollutant SMX was added to it, which contains inorganic anions and humic substances that may affect the degradation effect, so as to determine the performance of the system in real wastewater treatment as well as the selectivity of the non-radicals to the target pollutant [75]. Three-dimensional excitation-emission matrix fluorescence spectroscopy (3D-EEM) can distinguish humic-like, protein-like, microbial metabolites and other fluorescent components in the aquatic environment [76], and localize them by characteristic peaks (e.g.,  $\text{Ex}/\text{Em} = 270/450$  nm for humic-like peaks) [77]. The technique analyzes samples without complex pre-treatment and offers high analytical efficiency. Many organic contaminants are present in water at very low concentrations (e.g., pharmaceutical ingredients and their metabolites) and may not be accurately detected by conventional methods, while 3D-EEM provides highly sensitive analysis of these trace organic contaminants [78]. In this study, the transformation of organic matter in FeCoLDH/PMS system was monitored by this technique. The specific details of the technique are given in Text S1. The results of three-dimensional fluorescence and emission matrix fluorescence spectroscopy (3D-EEM) (Figure 12a–c) revealed typical fluorescence peaks ( $\text{EX}: 200\text{--}220$  nm;  $\text{EM}: 280\text{--}320$  nm) corresponding to humic acid-like organics in the raw wastewater. It can be seen from Figure 12b that after the addition of the target contaminant SMX, a new peak appears on the 3D-EEM, which can be matched with the characteristic peak of SMX [79]. These results demonstrate that the system not only efficiently degrades target pollutants in real wastewater but also effectively breaks down coexisting organic matter. In natural water treatment, challenges often arise from interfering substances, making the system's anti-interference ability critical for practical applications.

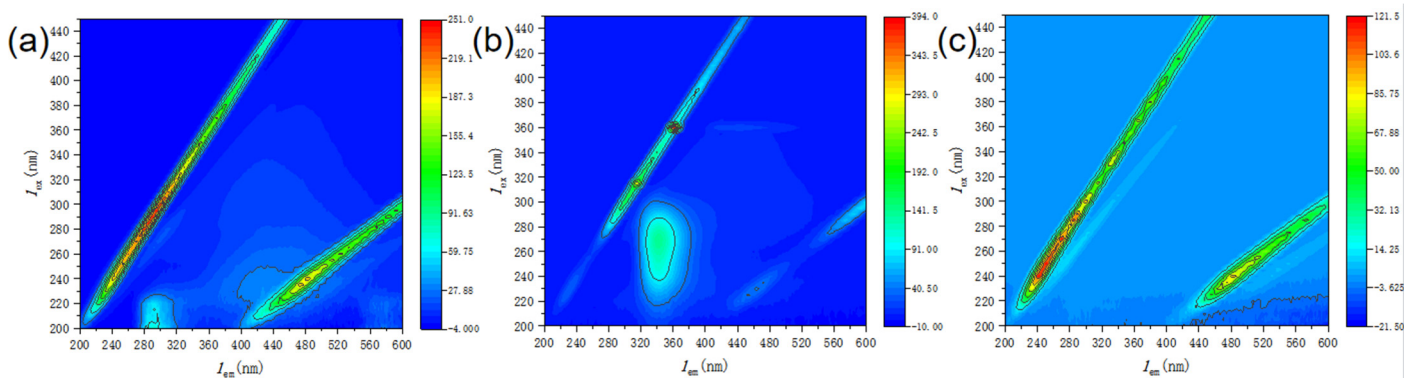


**Figure 12.** 3D-EEM fluorescence spectra of actual wastewater treated by FeCo-LDH/PMS system. Actual wastewater containing humus (**a**); with the addition of the target contaminant SMX (**b**); After degradation by FeCo-LDH/PMS system (**c**).

#### 4. Conclusions

High-valent iron-oxo species have been widely used in PMS-based systems due to their remarkable selectivity. However, their practical application is often limited by the need for strongly acidic or basic conditions. In this study, FeCo-LDH can establish a near-neutral pH microenvironment over a wide pH range (3.0–11.0) due to the proton buffering capacity of the amphiprotic hydroxide  $\text{Co}(\text{OH})_2$ . EPR tests and quenching experiments showed that  $\text{Fe(IV)=O}$  is the main reaction intermediate for pollutant degradation. The formation of a neutral pH microenvironment allowed for the sustained production and reaction of  $\text{Fe(IV)=O}$ , thus overcoming the traditional pH limitations associated with high-valent iron species in PMS systems. The practical value of the system is enhanced by its excellent long-term and cyclic stability, high selectivity for target contaminants, and deep treatment of real wastewater. This study provides new ideas to overcome the effect of acidic environment on the active components in the PMS-based system, reveals how the material can produce high-valent iron-oxo species, a strongly selective non-radical, and provides ideas and insights for its application in practical wastewater treatment.

**Supplementary Materials:** The following supporting information can be downloaded at: <https://www.mdpi.com/article/10.3390/app15095100/s1>, Text S1. Analysis method. Figure S1. The Fe 2p high-resolution spectra of FeCo-LDH (1:1). Figure S2. The Co 2p high-resolution spectra of FeCo-LDH (1:1). Figure S3. The Fe 2p high-resolution spectra of FeCo-LDH (1:2). Figure S4. The Co 2p high-resolution spectra of FeCo-LDH (1:2). Figure S5. Effect of PMS addition concentration on the degradation of SMX by FeCo-LDH + PMS system(catalyst: 0.1 g/L, SMX: 10 mg/L, PMS: 0.1–1 mM/L pH=5.66, T=25°C). Figure S6. Effect of SMX concentration on the degradation of SMX by FeCo-LDH+PMS system (catalyst: 0.1 g/L, SMX: 10–50 mg/L, PMS: 0.3 mM/L pH=5.66, T=25°C). Figure S7. Effect of catalyst dosing on the degradation of SMX by FeCo-LDH+PMS + PMS system (catalyst: 0.05–0.3 g/L, SMX: 10 mg/L, PMS: 0.3 mM/L pH=5.66, T=25°C). Figure S8. Conversion rates between pmso and pms $\text{O}_2$ . Figure S9. LC-MS mass spectra of SMX degradation intermediates. Figure S10. Effects of anions, humic acid, and different aqueous matrices on the degradation of SMX in the FeCo-LDH +PMS system. Figure S11. Degradation efficiency of SMX by mechanical mixing of various metal ions as well as hydroxides.

**Author Contributions:** Conceptualization, J.C.; Methodology, J.C.; Software, J.C.; Formal analysis, K.C.; Investigation, J.C.; Data curation, K.C.; Writing – original draft, J.C.; Writing – review & editing, J.C. and K.C.; Project administration, K.C. All authors have read and agreed to the published version of the manuscript.

**Funding:** This work was supported by Science and Technology Innovation Tackle Plan Project of Anhui Province (202423110050041) and The University Synergy Innovation Program of Anhui Province (GXXT-2023-046).

**Institutional Review Board Statement:** Not applicable.

**Informed Consent Statement:** Not applicable.

**Data Availability Statement:** All the data can be found in the manuscript and the Supplementary Material. Further requests can be directed to the corresponding author.

**Conflicts of Interest:** The authors declare no conflicts of interest.

## Reference

- Wang, F.N.; Guo, Z.B.; Qiao, X.B.; Fan, J.Y.; Li, W.; Mi, M.; Tao, Z.G.; He, M.C. Large deformation mechanism of thin-layered carbonaceous slate and energy coupling support technology of NPR anchor cable in Minxian Tunnel: A case study. *Tunn. Undergr. Space Technol.* **2021**, *117*, 104151.
- Tian, T.; Zhang, J.; Ge, S.; Tian, L. Enhanced gaseous benzene degradation by bimetallic MIL-101(Fe, Cu) activated persulfate system: Efficiency and mechanism. *Colloids Surf. A Physicochem. Eng. Asp.* **2025**, *706*, 135785.
- Sun, Y.; Huang, Y.; Zheng, S.; Chen, H.; Pei, J.; Yang, Y.; Ji, H.; Han, C. Critical review on the abatement of endocrine disrupting chemicals using synthesized iron-based materials in persulfate systems: Reactive species, reaction mechanisms, and perspectives. *Chem. Eng. J.* **2025**, *511*, 161675.
- Kim, S.-Y. Enhancing the degradation of 2,4-dinitrotoluene using zero-valent magnesium in the presence of persulfate and hydrogen peroxide. *J. Water Process Eng.* **2025**, *73*, 107485.
- Wang, Z.; Li, H.; Ma, W.; Wang, Y.; Cui, P.; Qi, J.; Chen, Z.; Zhu, Z.; Meng, F.; Highly efficient electro-catalysis activation of peroxymonosulfate by “used” As/Cr/Mo@FeOOH material for the degradation of metronidazole: Degradation mechanism and toxicity assessment. *J. Taiwan Inst. Chem. Eng.* **2021**, *121*, 302–312.
- Patel, A.; Raikar, L.G.; Gandhi, J.; Prakash, H. Degradation of cefixime antibiotic by continuous flow ultraviolet-C persulfate based advanced oxidation process: Fresh and marine water matrices, antibacterial activity removal, and cost analysis. *Chem. Eng. J.* **2025**, *512*, 162178.
- Lalas, K.; Panaras, G.; Souliotis, M.; Frontistis, Z. Degradation of micropollutants in water matrices using light activated—Persulfate: A review. *J. Environ. Manag.* **2025**, *373*, 123868.
- Bougouizi, N.; Ahmedchekkat, F.; Chihia, M. Heat and iron-activated persulfate for Orange G degradation: Kinetics and synergy effect studies. *Desalination Water Treat.* **2025**, *322*, 101090.
- Chen, T.; Liu, R.; Zhang, Y.; Shen, Y.; Yao, L.; Wang, X. Ultrasonic-activated persulfate treatment for enhancing pore volume and permeability of poplar wood. *Ind. Crops Prod.* **2025**, *227*, 120786.
- Meng, Z.; Li, C.; Zhao, G.; Yang, Y.; Yan, Y.; Hu, C.; Wang, W. Activation mechanism of persulfate by acidified oil shale semi-coke for catalytic degradation of volatile phenols: The synergistic effect of transition metal and surface organic matter. *J. Environ. Chem. Eng.* **2025**, *13*, 115780.
- Chen, W.; Zhang, J.; Hong, T.; Peng, X.; Fu, F. Dual heteroatom-doped porous biochar from chitosan/lignosulfonate gels for enhanced removal of tetracycline by persulfate activation: Performance and mechanism. *Int. J. Biol. Macromol.* **2025**, *295*, 139690.
- Xiong, Y.-H.; Pei, D.-S. A review on efficient removal of phthalic acid esters via biochars and transition metals-activated persulfate systems. *Chemosphere* **2021**, *277*, 130256.
- Hu, W.; Qin, X.; Lu, X.; Liu, Z.; Zhao, Y.; Yang, Y.; Zhen, G. Coupling weak magnetic field and zero-valent iron-activated persulfate oxidation process activation for improving dewaterability of waste activated sludge. *J. Water Process Eng.* **2024**, *64*, 105632.
- Duan, X.; Sun, H.; Shao, Z.; Wang, S. Nonradical reactions in environmental remediation processes: Uncertainty and challenges. *Appl. Catal. B: Environ.* **2018**, *224*, 973–982.
- Hu, P.; Long, M. Cobalt-catalyzed sulfate radical-based advanced oxidation: A review on heterogeneous catalysts and applications. *Appl. Catal. B: Environ.* **2016**, *181*, 103–117.
- Zhang, S.; Yin, Z.; Lu, Z.; Xu, Z.; Hu, C.; Li, F. A tandem dual-pathway non-radical water purification simultaneously induced by single-molecule peroxymonosulfate with a catalyst of coexisting Cu single atoms and Fe3C nanoparticles. *Chem. Eng. J.* **2024**, *500*, 157136.

17. Liu, L.; Li, Y.; Wang, K.; Zhu, C.; Li, Y.; Yang, N. A novel persulfate activation strategy by double Z-scheme  $\text{Bi}_2\text{O}_3/\text{CuBi}_2\text{O}_4/\text{BiOBr}$  heterojunction: Non-radical dominated pathway for levofloxacin degradation. *J. Environ. Chem. Eng.* **2024**, *12*, 114139.
18. Mazivila, S.J.; Ricardo, I.A.; Leitão, J.M.M.; da Silva, J.C.G.E. A review on advanced oxidation processes: From classical to new perspectives coupled to two- and multi-way calibration strategies to monitor degradation of contaminants in environmental samples. *Trends Environ. Anal. Chem.* **2019**, *24*, e00072.
19. Yang, X.; Zhang, P.; Hou, H.; Hu, J.; Liu, L.; Wu, L.; Chen, S.; Pan, K.; Liang, S.; Yuan, S.; et al. An iron chlorophyll derivative for enhanced degradation of bisphenol A: New insight into the generation mechanism of high-valent iron oxo species. *Chem. Eng. J.* **2023**, *451*, 138688.
20. Wang, Z.; Qiu, W.; Pang, S.-Y.; Zhou, Y.; Gao, Y.; Guan, C.; Jiang, J. Further understanding the involvement of Fe(IV) in peroxydisulfate and peroxyomonosulfate activation by Fe(II) for oxidative water treatment. *Chem. Eng. J.* **2019**, *371*, 842–847.
21. Lin, T.; Zhou, H.; Zhao, L.; Liang, S.; Luo, Y.; He, L.; Shan, S.; Hu, T.; Liu, Z.; Du, W. Direct generation of high-valent iron-oxo species to eliminate oxytetracycline at circumneutral pH via paper mill sludge ash activating peroxyomonosulfate. *Chem. Eng. J.* **2024**, *484*, 150021.
22. Li, Y.; Hu, J.; Bao, Y.; Xiao, Y.; Lin, L.; Li, B.; Li, X.-Y. High-valent iron-oxo species in heterogeneous catalysis: Formation, mechanism, and reactivity for the degradation of various emerging organic contaminants. *Chem. Eng. J.* **2024**, *501*, 157490.
23. Gagol, M.; Przyjazny, A.; Boczkaj, G. Highly effective degradation of selected groups of organic compounds by cavitation based AOPs under basic pH conditions. *Ultrason. Sonochemistry* **2018**, *45*, 257–266.
24. Huang, M.; Zhang, Y.; Xiang, W.; Zhou, T.; Wu, X.; Mao, J. Efficient adsorption of Mn(II) by layered double hydroxides intercalated with diethylenetriaminepentaacetic acid and the mechanistic study. *J. Environ. Sci.* **2019**, *85*, 56–65.
25. Zhu, Y.; Zhou, Y.; Zhang, T.; He, M.; Wang, Y.; Yang, X.; Yang, Y. Preparation and characterization of lactate-intercalated Co-Fe layered double hydroxides and exfoliated nanosheet film with low infrared emissivity. *Appl. Surf. Sci.* **2012**, *263*, 132–138.
26. Poudel, M.; Bustani, Z.; Li, X.; Zhu, J. Ring opening of cyclopropylmethylidene with trimethylaluminum: Synthesis of 1-cyclopropylethyl ether as an acid labile protecting group for hydroxyl Protection and carbohydrate synthesis. *J. Carbohydr. Chem.* **2025**, *44*, 81–93.
27. Kunimatsu, K.; Uchida, H.; Watanabe, M. Interactions between adsorbed hydrogen and water molecules on a polycrystalline Pt electrode studied by in-situ ATR-FTIR spectroscopy. *J. Electroanal. Chem.* **2024**, *954*, 118037.
28. Kristinaitytė, K.; Dagys, L.; Kausteklis, J.; Klimavicius, V.; Doroshenko, I.; Pogorelov, V.; Valevičienė, N.R.; Balevicius, V. NMR and FTIR studies of clustering of water molecules: From low-temperature matrices to nano-structured materials used in innovative medicine. *J. Mol. Liq.* **2017**, *235*, 1–6.
29. Yang, Q.; Zhong, Y.; Li, X.; Li, X.; Luo, K.; Wu, X.; Chen, H.; Liu, Y.; Zeng, G. Adsorption-coupled reduction of bromate by Fe(II)-Al(III) layered double hydroxide in fixed-bed column: Experimental and breakthrough curves analysis. *J. Ind. Eng. Chem.* **2015**, *28*, 54–59.
30. Liang, C.; Zhang, Y.; Shen, J.; Zhang, X.; Li, H.; Xie, S.; Li, Y.; Zhang, Z.C. High-performance overall water electrolysis enabled by a one-step fabricated bifunctional Pt/NiFe LDH catalyst on iron nickel foam. *Int. J. Hydrogen Energy* **2024**, *94*, 749–755.
31. Guo, P.; Xu, L.; Yu, T.; Zhao, P.; Xu, J.; Shen, B. Transition metal in-situ doped BiOBr: Introducing oxygen vacancies to enhance hydroxyl radical generation for improved photocatalytic degradation of toluene. *Sep. Purif. Technol.* **2025**, *354*, 129247.
32. Wei, Q.-X.; Zhang, A.-Y.; Yang, Z.; Hu, S.; Wang, D.-J.; Zhang, C.; Liu, C.; Liu, R. Oxygen-exfoliated cobalt-doped C<sub>3</sub>N<sub>4</sub> for superior Fenton-like catalysis: The accessible metal exposure and synergistic pollutant adsorption from three-dimensional layered configuration. *J. Environ. Chem. Eng.* **2023**, *11*, 111067.
33. Kalita, A.; Talukdar, A.K. Streamlined synthesis of iron and cobalt loaded MCM-48: High-performance heterogeneous catalysts for selective liquid-phase oxidation of toluene to benzaldehyde. *Heliyon* **2024**, *10*, e27296.
34. Li, Y.; Li, H.; Yang, M.; He, X.; Ni, P.; Kang, L.; Liu, Z.-H. Topochemical synthesis of  $\text{Ni}^{2+}\text{-Fe}^{3+}$  layered double hydroxides with large size. *Appl. Clay Sci.* **2011**, *52*, 51–55.
35. Zhang, H.; Yan, Z.; Wan, J.; Wang, Y.; Ye, G.; Huang, S.; Zeng, C.; Yi, J. Synthesis of Fe-N<sub>x</sub> site-based iron-nitrogen co-doped biochar catalysts for efficient removal of sulfamethoxazole from water by activation of persulfate: Electron transfer mechanism of non-free radical degradation. *Colloids Surf. A Physicochem. Eng. Asp.* **2022**, *654*, 130174.
36. Liu, Z.; Pan, S.; Xu, F.; Wang, Z.; Zhao, C.; Xu, X.; Gao, B.; Li, Q. Revealing the fundamental role of MoO<sub>2</sub> in promoting efficient and stable activation of persulfate by iron carbon based catalysts: Efficient  $\text{Fe}^{2+}\text{/Fe}^{3+}$  cycling to generate reactive species. *Water Res.* **2022**, *225*, 119142.
37. Sun, H.; Peng, X.; Zhang, S.; Liu, S.; Xiong, Y.; Tian, S.; Fang, J. Activation of peroxyomonosulfate by nitrogen-functionalized sludge carbon for efficient degradation of organic pollutants in water. *Bioresour. Technol.* **2017**, *241*, 244–251.

38. Duan, M.; Qiu, M.; Sun, S.; Guo, X.; Liu, Y.; Zheng, X.; Cao, F.; Kong, Q.; Zhang, J. Intercalating assembly of NiFe LDH nanosheets/CNTs composite as high-performance electrocatalyst for oxygen evolution reaction. *Appl. Clay Sci.* **2022**, *216*, 106360.
39. Liv, L.; Tosun, S.G. A novel perspective for estimating the passivation and energy storage characteristics in micro-mass coatings using CV, EIS, and EQCM techniques: Ultrahigh supercapacitor behaviors of Bismarck Brown R and Bismarck Brown Y polymer films. *J. Energy Storage* **2025**, *115*, 115985.
40. Mahato, N.; Singh, S.; Sreekanth, T.V.M.; Yoo, K.; Kim, J. Polycrystalline phases engineered in-situ in polyaniline-graphene composite evolving an exceptional stability and high charge storage capacity: An EIS investigative approach to evaluate material's stability. *J. Energy Storage* **2024**, *88*, 111464.
41. He, J.; Huang, J.; Wang, Z.; Liu, Z.; Chen, Y.; Su, R.; Ni, X.; Li, Y.; Xu, X.; Zhou, W.; et al. The enhanced catalytic degradation of sulfamethoxazole over Fe@nitrogen-doped carbon-supported nanocomposite: Insight into the mechanism. *Chem. Eng. J.* **2022**, *439*, 135784.
42. Bi, C.-C.; Ke, X.-X.; Chen, X.; Weerasooriya, R.; Hong, Z.-Y.; Wang, L.-C.; Wu, Y.-C.; Assembling reduced graphene oxide with sulfur/nitrogen-“hooks” for electrochemical determination of Hg(II). *Anal. Chim. Acta* **2020**, *1100*, 31–39.
43. Rachid, Y.; El-Asri, A.; El Gaayda, J.; Titchou, F.E.; Errami, M.; Aziz, J.; Yap, P.-S.; Abdelaziz, O.; Bakas, I.; Akbour, R.A. Adsorption of synthetic cationic dyes from water (experimental, DFT and Monte Carlo studies) and treatment of real industrial wastewater using dextrose compound-modified layered double hydroxide. *Process Saf. Environ. Prot.* **2024**, *194*, 1605–1624.
44. Nazir, M.A.; Bashir, M.A.; Najam, T.; Javed, M.S.; Suleman, S.; Hussain, S.; Kumar, O.P.; Shah, S.S.A.; Rehman, A.U. Combining structurally ordered intermetallic nodes: Kinetic and isothermal studies for removal of malachite green and methyl orange with mechanistic aspects. *Microchem. J.* **2021**, *164*, 105973.
45. Tian, H.; Peng, S.; Zhao, L.; Chen, Y.; Cui, K. Simultaneous adsorption of Cd(II) and degradation of OTC by activated biochar with ferrate: Efficiency and mechanism. *J. Hazard. Mater.* **2023**, *447*, 130711.
46. Ghiasi, S.; Mohammadi, T.; Tofiqhy, M.A. Hybrid nanofiltration thin film hollow fiber membranes with adsorptive supports containing bentonite and LDH nanoclays for boron removal. *J. Membr. Sci.* **2022**, *655*, 120576.
47. In-situ electro-generation and activation of hydrogen peroxide using a CuFeNLDH-CNTs modified graphite cathode for degradation of cefazolin. *J. Environ. Manag.* **2020**, *267*, 110629.
48. Ministry of Ecology and Environment of China & AQSIQ. (2010). Emission Standard of Pollutants for Copper, Nickel, Cobalt Industry (GB 25467-2010/XG1-2013). Beijing: China Environmental Science Press.
49. Cheng, C.; Ren, W.; Zhang, H.; Duan, X.; Wang, S. Single-atom iron catalysts for peroxyomonosulfate-based advanced oxidation processes: Coordination structure versus reactive species. *Chin. J. Catal.* **2024**, *59*, 15–37.
50. Wu, X.; Liu, T.; Ni, W.; Yang, H.; Huang, H.; He, S.; Li, C.; Ning, H.; Wu, W.; Zhao, Q.; et al. Engineering controllable oxygen vacancy defects in iron hydroxide oxide immobilized on reduced graphene oxide for boosting visible light-driven photo-Fenton-like oxidation. *J. Colloid Interface Sci.* **2022**, *623*, 9–20.
51. Wang, Y.; Huang, Y.; Chen, Y.; Dou, L.; Ren, Y.; Li, N.; Lai, B.; Tan, B. Cobalt doped g-C3N4 activated peroxyomonosulfate for organic pollutant degradation: Alterations in cobalt species and reactive oxygen species. *Chemosphere* **2024**, *369*, 143763.
52. Zhang, H.; Smith, J.R.L.; Shen, F.; Qi, X. ZnFe layered double hydroxide wrapped metal-organic framework derived cobalt-nitrogen-doped carbon material as peroxyomonosulfate activator for ciprofloxacin degradation. *Chem. Eng. J.* **2024**, *496*, 154191.
53. Wang, S.; Deng, Y.; Shao, B.; Zhu, J.; Guan, X. Reinvestigation of the oxidation of organic contaminants by Fe(VI): Kinetics and effects of water matrix constituents. *J. Hazard. Mater.* **2022**, *430*, 128421.
54. Zou, Y.; Fu, S.; Xu, Z.; Zhou, X.; Li, J.; Zhang, Y.; Lu, Y.; Li, S.; Zhang, T. Unveiling the long-range interaction of sulfur in the second shell of Fe-N4 single-atom sites for highly selective generation of high-valent iron-oxo species in peroxyomonosulfate activation. *Chem. Eng. J.* **2025**, *505*, 159684.
55. Zhou, X.; Yin, R.; Kang, J.; Li, Z.; Pan, Y.; Bai, J.; Li, A.J.; Qiu, R. Atomic cation-vacancy modulated peroxyomonosulfate nonradical oxidation of sulfamethoxazole via high-valent iron-oxo species. *Appl. Catal. B Environ.* **2023**, *330*, 122640.
56. Liu, L.; Wang, A.; Hu, J.; Hou, H.; Liang, S.; Yang, J. Peroxyomonosulfate activated by natural porphyrin derivatives for rapid degradation of organic pollutants via singlet oxygen and high-valent iron-oxo species. *Chemosphere* **2023**, *331*, 138783.
57. Wang, J.; Wang, S. Reactive species in advanced oxidation processes: Formation, identification and reaction mechanism. *Chem. Eng. J.* **2020**, *401*, 126158.
58. Wang, X.; Gong, W.; Zhu, J.; Peng, G. New insights into the quantification of Fe(IV) using methyl phenyl sulfoxide (PMSO) as probe in the iron-based heterogeneous catalyst activated persulfate process. *Environ. Pollut.* **2024**, *362*, 124924.

59. Cao, S.; Yin, Y.; Zheng, S.; Song, C.; Gan, X.; Zhang, W.; Feng, D.; Shang, J.; Cheng, X. Peroxymonosulfate activation by Ni–Co nanoparticles encapsulated in nitrogen-doped carbon derived from Co-doped Ni metal–organic frameworks for efficient enrofloxacin degradation. *Chem. Eng. J.* **2025**, *503*, 158281.
60. Li, Y.; Yang, T.; Qiu, S.; Lin, W.; Yan, J.; Fan, S.; Zhou, Q. Uniform N-coordinated single-atomic iron sites dispersed in porous carbon framework to activate PMS for efficient BPA degradation via high-valent iron-oxo species. *Chem. Eng. J.* **2020**, *389*, 124382.
61. Wang, N.; Hsu, C.; Zhu, L.; Tseng, S.; Hsu, J.-P. Influence of metal oxide nanoparticles concentration on their zeta potential. *J. Colloid Interface Sci.* **2013**, *407*, 22–28.
62. Ulu, F.; Gencen, E.; Kobya, M. Removal of natural organic matter from Lake Terkos by EC process: Studying on removal mechanism by floc size and zeta potential measurement and characterization by HPSEC method. *J. Water Process Eng.* **2019**, *31*, 100831.
63. Joshua, A.M.; Ooi, E.H.; Chang, W.S.; Lau, E.V. Mechanical and physicochemical characteristics of sub-millimeter and macro-bubbles: Insights from AFM analysis, zeta potential measurements and rise velocity. *Results Surf. Interfaces* **2024**, *16*, 100262.
64. Wang, Y.; Deng, Y.; Yao, L.; Yang, X. Colloid-bound radicals formed in NOM-enhanced Fe(III)/peroxymonosulfate process accelerate the degradation of trace organic contaminants in water. *Water Res.* **2024**, *248*, 120880.
65. Qi, C.; Yu, G.; Huang, J.; Wang, B.; Wang, Y.; Deng, S. Activation of persulfate by modified drinking water treatment residuals for sulfamethoxazole degradation. *Chem. Eng. J.* **2018**, *353*, 490–498.
66. Zhi, K.; Liu, D.; Xu, J.; Li, Z.; Li, S.; Luo, L.; Gong, G.; Han, R.; Yin, A.; Guo, L. N-doped graphene loaded with Ru sites as PMS activators for SMX degradation via non-radical pathway: Efficiency, selectivity and mechanism. *Chem. Eng. J.* **2025**, *512*, 162230.
67. Yang, W.; Dong, H.; Tian, Y.; Tong, Y.; Lu, J.; Liao, L.; Niu, J. Electrochemistry enhanced multi-stage biological contact oxidation treating sulfamethoxazole wastewater: Performance, degradation pathway and microbial community. *Sep. Purif. Technol.* **2025**, *357*, 130044.
68. Xia, X.; Gao, Q.; Ji, X.; Wan, J.; Wang, Y.; Ma, Y. Novel cobalt-doped CuFe<sub>2</sub>O<sub>4</sub> spinel catalyst for enhanced peroxymonosulfate activation to achieve rapid degradation of tetracycline hydrochloride: Dominant roles of O<sub>2</sub><sup>-</sup> and 1O<sub>2</sub> in the oxidation process. *J. Water Process Eng.* **2025**, *69*, 106638.
69. Tian, M.; Ren, X.; Fu, N.; Chen, Z.; Wei, Y.; Fan, X.; Yang, Z.; An, J. Ethylene glycol-assisted synthesis of Mo/Fe co-doped g-C<sub>3</sub>N<sub>4</sub> composite 8-CNMF12 efficiently activates PMS to degrade phenol. *Colloids Surf. A Physicochem. Eng. Asp.* **2025**, *709*, 136134.
70. Sun, Z.; Zhao, M.; Zhou, X. Reliability analysis of NaN<sub>3</sub> as quencher of 1O<sub>2</sub> in heterogeneous persulfate catalytic oxidation system. *Catal. Commun.* **2023**, *183*, 106774.
71. Deng, X.; Yang, H.; Zhao, D.; Guan, J.; Gu, Z.; Zhang, L. Mn–Cu co-doped graphitic carbon nitride accelerates permonosulfate to generate more singlet oxygen in pollutant degradation. *J. Water Process Eng.* **2024**, *64*, 105755.
72. Su, S.; Guo, W.; Leng, Y.; Yi, C.; Ma, Z. Heterogeneous activation of Oxone by Co(<sub>x</sub>)Fe(<sub>3-x</sub>)O<sub>4</sub> nanocatalysts for degradation of rhodamine B. *J. Hazard. Mater.* **2013**, *244–245*, 736–742.
73. Feng, Y.; Liao, C.; Kong, L.; Wu, D.; Liu, Y.; Lee, P.-H.; Shih, K. Facile synthesis of highly reactive and stable Fe-doped g-C<sub>3</sub>N<sub>4</sub> composites for peroxymonosulfate activation: A novel nonradical oxidation process. *J. Hazard. Mater.* **2018**, *354*, 63–71.
74. Shen, Y.; de Vidales, M.J.M.; Gorni, G.; Gómez-Herrero, A.; Fernández-Martínez, F.; Dos santos-García, A.J. Enhanced performance and recyclability for peroxymonosulfate activation via g-C<sub>3</sub>N<sub>4</sub> supported CoFe layer double oxide. *Chem. Eng. J.* **2022**, *444*, 136610.
75. Yan, H.; Xu, L.; Wei, H.; Li, X. Biotransformation of sulfamethoxazole by newly isolated surfactant-producing strain *Proteus mirabilis* sp. ZXY4: Removal efficiency, pathways, and mechanisms. *Bioresour. Technol.* **2023**, *385*, 129422.
76. Zhu, Y.-Y.; Liu, Y.; Xu, J.; Ni, B.-J. Three-dimensional excitation-emission matrix (EEM) fluorescence approach to probing the binding interactions of polystyrene microplastics to bisphenol A. *J. Hazard. Mater. Adv.* **2022**, *5*, 100046.
77. Zhang, F.; Wang, X.; Chen, Y.; Airiken, M. Estimation of surface water quality parameters based on hyper-spectral and 3D-EEM fluorescence technologies in the Ebinur Lake Watershed, China. *Phys. Chem. Earth Parts A/B/C* **2020**, *118–119*, 102895.
78. Zhang, R.; Liu, J.; Gao, B.; Sillanpää, M. The effect of autochthonous metal ions and humic substances on landfill leachate ozonation: Reactive oxygen species and 3D fluorescence analysis. *Sep. Purif. Technol.* **2025**, *354*, 129433.
79. Roy, N.; Roy, S.; Debroy, A.; Mukherjee, A. *Chlorella* sp. EPS loaded alginate microsphere: A novel bionanomaterial for adsorptive removal of sulfamethoxazole from the aqueous solutions. *Environ. Technol. Innov.* **2024**, *33*, 103513.